

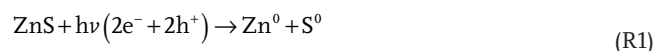
# Alumina-Protected, Durable and Photostable Zinc Sulfide Particles from Scalable Atomic Layer Deposition

Thomas Lange, Sven Reichenberger, Markus Rohe, Mathias Bartsch, Laura Kampermann, Julian Klein, Jennifer Strunk, Gerd Bacher, Robert Schlögl, and Stephan Barcikowski\*

Zinc sulfide has unique and easily modifiable photophysical properties and is a promising candidate for photocatalysis and optoelectronic devices. However, ZnS suffers from corrosive decomposition during excitation processes like UV irradiation, which drastically limits its field of potential applications. For the first time, complete photostabilization of individual ZnS particles by a dense, durable, and only 3-nm-thick Al<sub>2</sub>O<sub>3</sub> layer, produced by rotary atomic layer deposition (ALD) is reported. In contrast to bare ZnS, the coated particles do not suffer from photocorrosive degradation even under long-term or high power UV irradiation. The presence of a protection layer covering the entire ZnS surface is additionally confirmed by microscopic and spectroscopic investigations of particle cross-sections. Further, complete inhibition of the reaction between Ag<sup>+</sup> ions added as the analyte and the ZnS surface is observed. Durability tests of the as-prepared Al<sub>2</sub>O<sub>3</sub> layer upon prolonged exposure to water reveal a significant decrease in the protection capability of the layer, which is ascribed to the hydrolysis of the amorphous Al<sub>2</sub>O<sub>3</sub>. A calcination step at 1000 °C after the ALD treatment, which leads to crystallization of the amorphous Al<sub>2</sub>O<sub>3</sub> layer, successfully suppresses this hydrolysis and produces an insulating, dense, and inert protection layer.

in recent years.<sup>[1]</sup> In particular, the white n-type semiconductor zinc sulfide has attracted much interest as photocatalyst<sup>[2]</sup> or component for optoelectronic devices<sup>[3]</sup> (such as field emission displays (FED),<sup>[4]</sup> light emitting diodes,<sup>[5]</sup> or solar cells<sup>[6]</sup>) as a consequence of its wide bandgap, high optical transmittance for visible light, good electron mobility, and a fast and efficient charge carrier formation. Furthermore, ZnS exhibits a low Mohs hardness, good opacity, and can be easily produced on a ton scale, which allows its application as white pigment<sup>[7]</sup> and polymer additive.<sup>[8]</sup> Unfortunately, ZnS is very susceptible to thermodynamically highly favored oxidation during excitation processes such as UV irradiation or electron beam bombardment under humid conditions causing its degradation to ZnSO<sub>4</sub>, ZnO, or Zn<sup>0</sup>.<sup>[4,9]</sup> This corrosion process severely impairs the use of ZnS in various applications due to a loss of activity (photocatalyst<sup>[10]</sup>), darkening of the surface (pigment<sup>[11]</sup>), and decrease

of luminescence intensity (FED,<sup>[4]</sup> and light-emitting quantum dots (QD)<sup>[12]</sup>). For photocorrosive decomposition of ZnS, the following degradation mechanism was found:<sup>[9]</sup>




## 1. Introduction

Due to easily tunable optical, chemical, and electronic properties as well as low production costs, metal sulfides gained increasing attention for optoelectronic and renewable energy applications

T. Lange, Dr. S. Reichenberger, Prof. S. Barcikowski  
Technical Chemistry I and Center for Nanointegration Duisburg-Essen (CENIDE)  
University of Duisburg-Essen  
Universitätsstraße 7, Essen 45141, Germany  
E-mail: stephan.barcikowski@uni-due.de

Dr. M. Rohe  
Venator Germany GmbH  
Dr.-Rudolf-Sachtleben-Straße 4, Duisburg 47198, Germany

M. Bartsch  
Experimental Physics  
University of Duisburg-Essen  
Lotharstraße 1, Duisburg 47057, Germany  
L. Kampermann, J. Klein, Prof. G. Bacher  
Werkstoffe der Elektrotechnik and Center for Nanointegration  
Duisburg-Essen (CENIDE)  
University of Duisburg-Essen  
Bismarckstraße 81, Duisburg 47057, Germany  
Prof. J. Strunk  
Leibniz Institute for Catalysis  
Albert-Einstein-Straße 29A, Rostock 18059, Germany  
Prof. R. Schlögl  
Max Planck Institute for Chemical Energy Conversion  
Stiftstraße 34-16, Muelheim an der Ruhr 45470, Germany

 The ORCID identification number(s) for the author(s) of this article can be found under <https://doi.org/10.1002/adfm.202009323>.

© 2021 The Authors. Advanced Functional Materials published by Wiley-VCH GmbH. This is an open access article under the terms of the Creative Commons Attribution-NonCommercial-NoDerivs License, which permits use and distribution in any medium, provided the original work is properly cited, the use is non-commercial and no modifications or adaptations are made.

DOI: 10.1002/adfm.202009323



A possible stabilization approach reported in the literature is transition metal (e.g., Co or Ni)<sup>[7a,9i,j,13]</sup> or non-metal<sup>[14]</sup> doping to reduce the amount or oxidative power of photogenerated charge carriers, respectively. However, as the excited charge carriers are driving the chemical photocatalytic or optoelectronic processes, these stabilization approaches impair corresponding applications of ZnS. Moreover, heavy metals such as Ni or Co are critical elements in terms of environmental sustainability and their use should be minimized as much as possible.<sup>[15]</sup> An alternate route to circumvent the aforementioned disadvantage of the presented routes is to separate the ZnS surface from the water molecules, which are mandatory for self-decomposition. This passivation can be achieved by introducing a transparent, sufficiently thick, and dense protection coating. One of the most precise methods to deposit tailored, uniform, and nearly pinhole-free layers with thickness-resolution on the nm-scale is the atomic layer deposition (ALD) of inorganic materials, which was initially developed and established for the deposition of electroluminescent ZnS films in the 1970s.<sup>[16]</sup> For the fabrication of electroluminescent devices, these ZnS films were embedded between two oxide films (such as Al<sub>2</sub>O<sub>3</sub> or Ta<sub>2</sub>O<sub>5</sub>), which act as ion barrier, dielectric, and passivation layer.<sup>[17]</sup> Furthermore, the stabilization of sulfide nanoparticles for optoelectronic applications by oxide passivation layers has been reported in the literature, but these nanoparticles were also deposited as films on flat substrates before being coated.<sup>[12,18]</sup> In contrast to the oxide coating of sulfide films, the stabilization approach of a 3D encapsulation of individual sulfide particles is much more challenging. However, such individual coated particles have a high application potential as they, for example, can be loaded with plasmonic nanoparticles, incorporated into matrixes (like polymers), or fixated onto various substrates. The deposition of Al<sub>2</sub>O<sub>3</sub>, considered to be the best available ALD process<sup>[17e]</sup>, is one of the most common approaches for coating such sulfide films composed of nanoparticles.<sup>[12,18]</sup> Here, Cheng et al. reported a coating of CdSe/ZnS core/shell QD which were deposited on a flat SiO<sub>2</sub> substrate subsequently being covered with a 10-nm-thick layer of Al<sub>2</sub>O<sub>3</sub> by thermal ALD. The coated QD film was successfully protected against photodegradation in ambient air as shown by photoluminescence (PL) measurements under high power UV irradiation.<sup>[12]</sup> Buonsanti et al. coated a moisture-sensitive perovskite QD film with Al<sub>2</sub>O<sub>3</sub> by ALD and obtained a highly stable luminescent film even when immersed in water for 1 h.<sup>[19]</sup> Furthermore, PbS and PbSe QD films were successfully passivated by Al<sub>2</sub>O<sub>3</sub> layers with thicknesses up to 130 nm and retained their photophysical properties for at least 60 days even under prolonged exposure to ambient air.<sup>[18a,b,d,20]</sup> Thus, despite the susceptibility of Al<sub>2</sub>O<sub>3</sub> to moisture/water reported in the literature,<sup>[21]</sup> it is still capable to provide sufficient protection for the underlying surfaces, even under humid conditions and intensive UV irradiation. Liu et al. coated CdS nanoparticles with Al<sub>2</sub>O<sub>3</sub> by only one ALD cycle, to protect the surface without inhibiting the charge carrier transportation through a thick passivation layer.<sup>[22]</sup> They observed a

significant increase of the photocatalyst lifetime after the ALD treatment, but the dye degradation rate decreased by 30% after the fourth reuse cycle (14 h of illumination) and X-ray photoelectron spectroscopy (XPS) analysis revealed traces of CdSO<sub>4</sub>, indicating incomplete photostabilization. However, a determination of the thinnest Al<sub>2</sub>O<sub>3</sub> layer, which completely protects sulfide surfaces, as well as long-term durability tests of the coating have not yet been carried out. A 3D protection layer that is relevant for photocatalytic, optoelectronic, or pigment applications should be as thin as possible but still dense, and must also have a high durability to ensure sufficient long-term stability. Thus, the aforementioned investigations are highly required.

For the first time, we demonstrate completely photostabilized ZnS particles covered by a dense and durable Al<sub>2</sub>O<sub>3</sub> layer, about 3 nm thick, deposited by rotary ALD in gram scale. A high photostability and an entire encapsulation of the exposed ZnS surface were confirmed utilizing spectroscopic, microscopic, and chemical investigations. Furthermore, long-term stability tests under harsh conditions were performed to investigate to what extent the water sensitivity of Al<sub>2</sub>O<sub>3</sub> affects its passivation capacity. It was revealed that the hydrolysis of the deposited Al<sub>2</sub>O<sub>3</sub> enabled the penetration of H<sub>2</sub>O and Ag<sup>+</sup> ions, which in turn can be inhibited by a crystallization of the as-prepared amorphous Al<sub>2</sub>O<sub>3</sub> layer.

## 2. Results and Discussion

### 2.1. Suppression of Photocorrosion by ALD-Al<sub>2</sub>O<sub>3</sub>

Figure 1 shows the influence of the temperature during the ALD process (25 cycles) on the PL intensity of coated and bare ZnS in the presence of water. The uncoated ZnS shows a significant emission between 400 and 600 nm, most likely due to self-activated (SA) centers and/or Cu-interstitials (B-Cu) originating from trace amounts of chloride and/or copper, respectively,<sup>[23]</sup> which are common impurities in industrially produced undoped ZnS as reported in ref. [24]. For uncoated ZnS, the PL band decreases significantly with UV illumination time due to photocorrosion (R1–R4) of ZnS in the presence of water (Figure 1a). This photocorrosion-related intensity decrease can be attributed to a gradual decomposition of the surface and the scattering and absorption of the excitation and luminescent light by the formed Zn<sup>0</sup>.<sup>[25]</sup> However, for the ZnS particles which were previously coated at 150 °C, the PL intensity is maintained during UV irradiation and the illuminated area remains white (Figure 1b). Thus, the photocorrosive Zn<sup>0</sup> formation was successfully prevented by the ALD treatment at 150 °C in line with previous reports.<sup>[12]</sup> The corresponding normalized PL peak integrals for ZnS before and after the ALD process at 100, 150, and 200 °C are shown in Figure 1c). The coating at 100 °C leads to an enhanced photostability compared to the uncoated ZnS, as the relative PL intensity after 90 min of UV irradiation is increased from 7% to about 22%. However, a complete suppression of photocorrosion is not achieved. A successful prevention from photocorrosive Zn<sup>0</sup> formation only becomes apparent at 150 or 200 °C, as about 96% of the initial PL intensity is maintained after 90 min of UV irradiation, which is also in line with a much higher Al<sub>2</sub>O<sub>3</sub> weight loading of 5.5 wt% quantified by

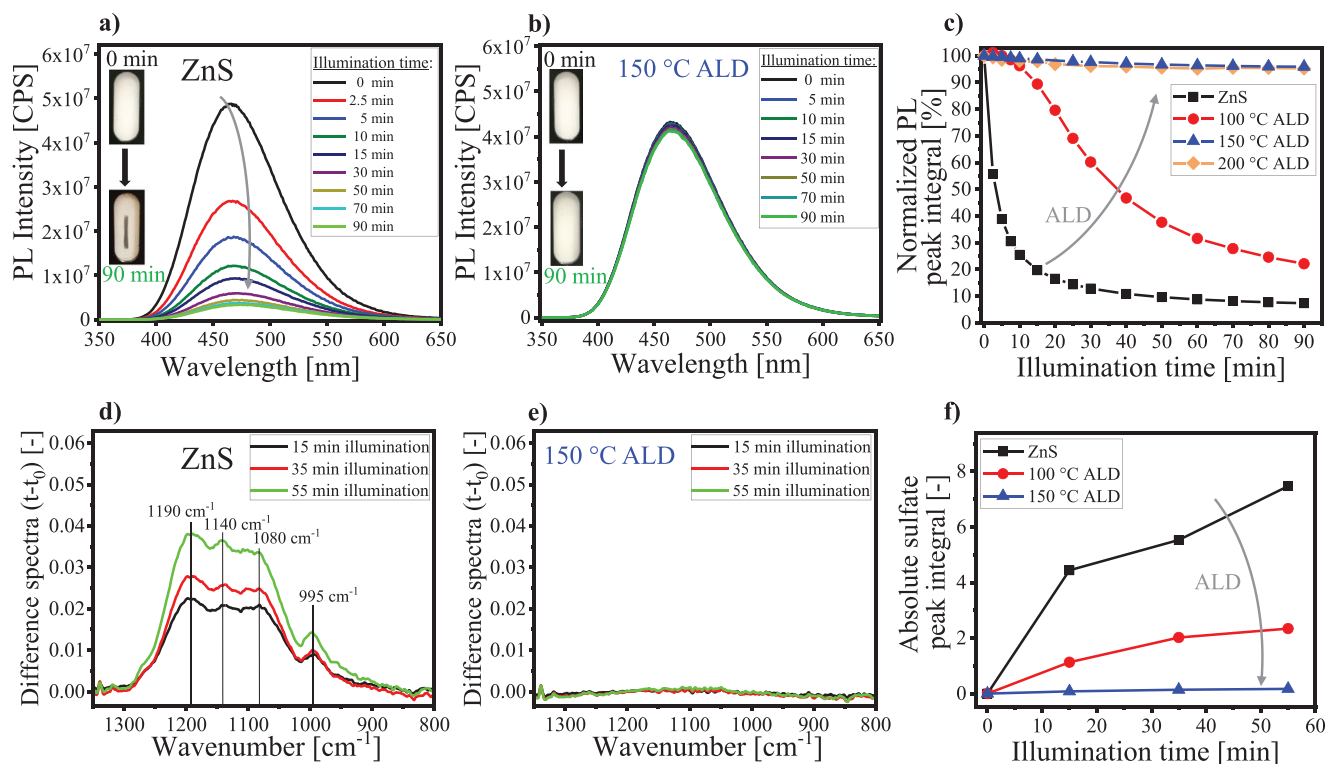


**Figure 1.** ALD countering effects: Photocorrosive  $\text{Zn}^0$  formation shown in PL spectra during prolonged UV-illumination of ZnS a) before and b) after ALD treatment at 150 °C. The dimensions of the illuminated areas shown in the inset pictures are 15 mm  $\times$  100 mm. c) Normalized PL peak integral upon prolonged UV illumination of ZnS before and after ALD treatment at 100, 150, and 200 °C. Photocorrosive sulfate formation shown in difference spectra after UV illumination for 15, 35, and 55 min of ZnS d) before and e) after ALD treatment at 150 °C. f) Integrated area of the sulfate peak regime (1050 to 1300  $\text{cm}^{-1}$ ) as a function of the UV illumination time.

acid digestion and subsequent inductively coupled plasma mass spectrometry (ICP-MS) (see Table 1).

To investigate whether both, photocorrosive  $\text{Zn}^0$  and  $\text{SO}_4^{2-}$  formation were successfully suppressed, the UV light-induced formation of sulfates was investigated by diffuse reflectance infrared Fourier transform spectroscopy (DRIFTS). Based on the IR spectra (see Figure S1, Supporting Information), and the thereof calculated difference spectra between neat ZnS (no ALD) before and after UV light treatment, a formation of  $\text{SO}_4^{2-}$  is clearly visible after 15, 35, and 55 min of UV illumination in the wavenumber range of about 1050 to 1300  $\text{cm}^{-1}$  (Figure 1d).<sup>[26]</sup>

The difference spectra show four IR peaks that can be attributed to the asymmetric, triply degenerated S–O stretching vibration  $\nu_3$  located at about 1190, 1140, and 1080  $\text{cm}^{-1}$  and the symmetric S–O stretching vibration  $\nu_1$  located at 995  $\text{cm}^{-1}$ , which becomes IR active due to a reduced symmetry of the sulfate ion upon coordination to a metal cation.<sup>[27]</sup> The integrated area of the sulfate peak regime for the uncoated ZnS shows a pronounced increase under prolonged UV irradiation (Figure 1f).

**Table 1.** Deposited weight loading of  $\text{Al}_2\text{O}_3$  in dependence of the deposition temperature during the ALD treatment.

	ZnS	100 °C ALD	150 °C ALD	200 °C ALD
Weight loading $\text{Al}_2\text{O}_3$ [wt%]	0	0.6	5.5	5.4

The amount of  $\text{Al}_2\text{O}_3$  was calculated based on the quantified Al amount found by acid digestion and subsequent ICP-MS analysis.

However, the photocorrosive formation of  $\text{SO}_4^{2-}$  is significantly suppressed after ALD treatment at 100 °C and completely inhibited after treatment at 150 °C. Consequently, a temperature of at least 150 °C is required to deposit  $\text{Al}_2\text{O}_3$  in sufficient quantities on the ZnS particles and protect its surface from photocorrosion. The deposition of only small amounts of  $\text{Al}_2\text{O}_3$  at 100 °C may be related to an insufficient thermal activation and reaction of the aluminum precursor (trimethylaluminum, TMA) with the ZnS surface sites during ALD.<sup>[16c,28]</sup> When comparing our results to literature on  $\text{Al}_2\text{O}_3$  deposition onto Si(100) surfaces, the growth rate and hence deposited mass should only be reduced by about 10% when lowering the temperature from about 150 to 100 °C.<sup>[16c,28a]</sup> In turn, we observe a decrease of the deposited  $\text{Al}_2\text{O}_3$  weight loading of about 90% (see Table 1), such that different thermal activation barriers for the respective surface sites might play a crucial role. FTIR measurements of ZnS showed that  $\equiv\text{Zn}-\text{OH}$  groups are present on the surface at 150 °C under vacuum,<sup>[26]</sup> which will probably act as active surface sites for the reaction with TMA. These  $\equiv\text{Zn}-\text{OH}$  groups are less acidic ( $\text{p}K_a \approx 11$ <sup>[29]</sup>) than  $\equiv\text{Si}-\text{OH}$  groups ( $\text{p}K_a \approx 7$ <sup>[30]</sup>), indicating a lower reactivity towards the protonation of TMA and therefore may require a higher thermal activation energy, which seems to be provided at a temperature of at least 150 °C. Since the deposited weight loading of  $\text{Al}_2\text{O}_3$  was found to only show a weak temperature dependence between 150 and 200 °C (Table 1), this temperature regime appears to be an acceptable temperature window for ALD growth.

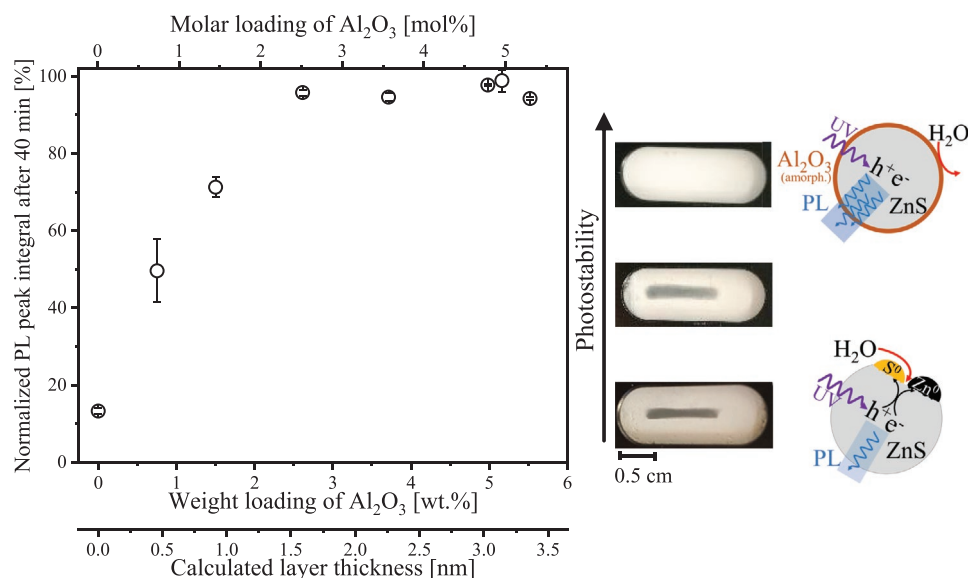


**Figure 2.** Corrosion resistance: Normalized PL peak integral after 40 min of UV illumination as a function of the deposited Al amount and the calculated layer thickness (left). The amount of Al<sub>2</sub>O<sub>3</sub> was calculated based on the quantified Al amount found by acid digestion and subsequent ICP-MS analysis. Images after the UV illumination of ZnS with 0, 1.0, and 2.6 wt% Al<sub>2</sub>O<sub>3</sub> (bottom to top) (right).

To identify the smallest amount of Al<sub>2</sub>O<sub>3</sub>, deposited at 150 °C, for the thinnest possible but still protective layer, a variation of the ALD cycle number with subsequent Al quantification was carried out. **Figure 2** shows the normalized PL intensity after 40 min of UV illumination as a function of the deposited Al amount. Based on the molar density of Al<sub>2</sub>O<sub>3</sub>, the BET surface of the ZnS particles, and the deposited mass of Al, the theoretical layer thickness  $d$  was calculated using Equation (1) under the assumption of spherical particle shapes (derivation see Equations S1–S4, Supporting Information)

$$V_L = S_{\text{BET}} \times d = \frac{n_{\text{Al}}}{\rho_{\text{molar}}} \rightarrow d = \frac{n_{\text{Al}}}{\rho_{\text{molar}} \times S_{\text{BET}}} \quad (1)$$

where  $V_L$  is the volume of the deposited layer,  $S_{\text{BET}}$  the BET surface area of ZnS before coating (4.8 m<sup>2</sup> g<sup>-1</sup>),  $d$  the thickness of the layer,  $n_{\text{Al}}$  the amount of deposited Al<sub>2</sub>O<sub>3</sub> and  $\rho_{\text{molar}}$  the molar density of Al<sub>2</sub>O<sub>3</sub> produced by ALD (3.433 × 10<sup>4</sup> mol m<sup>-3</sup> ≙ 3.5 g cm<sup>-3</sup>).<sup>[28a,b,31]</sup> As can be seen from **Figure 2**, an increasing photostability can be observed with increasing Al<sub>2</sub>O<sub>3</sub> loading from 0 to 5.5 wt%, reaching a complete suppression of photocorrosion already at 2.6 wt% Al<sub>2</sub>O<sub>3</sub>, which corresponds to a calculated layer thickness of about 1.6 nm. Furthermore, the plot of the theoretical layer thickness as a function of the ALD cycle number (see **Figure S2**, Supporting Information) gives a growth rate of 1.3 Å cycle<sup>-1</sup>, which matches very well with values for Al<sub>2</sub>O<sub>3</sub> growth of about 1.1–1.3 Å cycle<sup>-1</sup> reported in the literature.<sup>[16b,c,32]</sup>

## 2.2. In-Depth Characterization of the Alumina Layer

Focused ion beam (FIB) lamella cross-sections of the coated ZnS sub-microparticles were investigated by energy-dispersive X-ray spectroscopy (EDX) line scans and transmission electron

microscopy (TEM). **Figure 3** exemplarily shows the surface of an uncoated (a) and coated (b) ZnS particle. The TEM images in **Figure 3a,b** reveal the additional presence of a surface layer for the coated particle compared to the untreated ZnS. According to the EDX line scan (**Figure 3d**), the deposited layer consists of an Al- and O-containing species and has a thickness of about 3.4 nm (**Figure 3b** inset), which corresponds to a growth rate of about 1.4 Å cycle<sup>-1</sup> in line with the literature<sup>[16b,c,32]</sup> and the previously calculated growth rate (see **Figure S2**, Supporting Information). Based on the line plot of the gray value, a lattice spacing of 0.32 nm is found for the mixed-phase ZnS, which corresponds to the [002] or [111] plane of hexagonal wurtzite (ZnS(W))<sup>[33]</sup> or cubic sphalerite (ZnS(S)),<sup>[34]</sup> respectively, with reported lattice spacings of about 3.1 Å.

While high-resolution TEM (HR-TEM) analysis confirms the successful formation of Al<sub>2</sub>O<sub>3</sub> film around a representative ZnS particle, it still remains to be proven whether this is true for the whole ensemble. Therefore, the layer density of 50 mg of encapsulated ZnS (equal to ≈ 3.1 × 10<sup>19</sup> particles) was chemically examined using a silver nitrate solution to quantify the amount of still accessible ZnS surface sites. The ZnS surface is very sensitive to Ag<sup>+</sup> ions, which leads to an immediate formation of brown Ag<sub>2</sub>S and the release of Zn<sup>2+</sup> ions until one of the reactants is completely consumed.<sup>[35]</sup> **Figure 3e** shows the loss of ZnS after the storage in a 0.1 M AgNO<sub>3</sub> solution for 1 and 5 h as a function of the weight loading of Al<sub>2</sub>O<sub>3</sub> on ZnS. For the uncoated ZnS, about 16.2 and 22.5 mol% of ZnS leached into the AgNO<sub>3</sub> solution after 1 and 5 h, respectively. This is additionally supported by X-ray diffraction (XRD) (see **Figure S3**, Supporting Information) which shows the presence of Ag<sub>2</sub>S in the subsequently dried powder. With increasing mass load of Al<sub>2</sub>O<sub>3</sub> covering the ZnS surface, the dissolution of ZnS and formation of brown Ag<sub>2</sub>S is significantly reduced and completely inhibited for an Al<sub>2</sub>O<sub>3</sub> mass load of ≥ 2.6 wt%. This threshold mass load is in perfect agreement with the previously found,



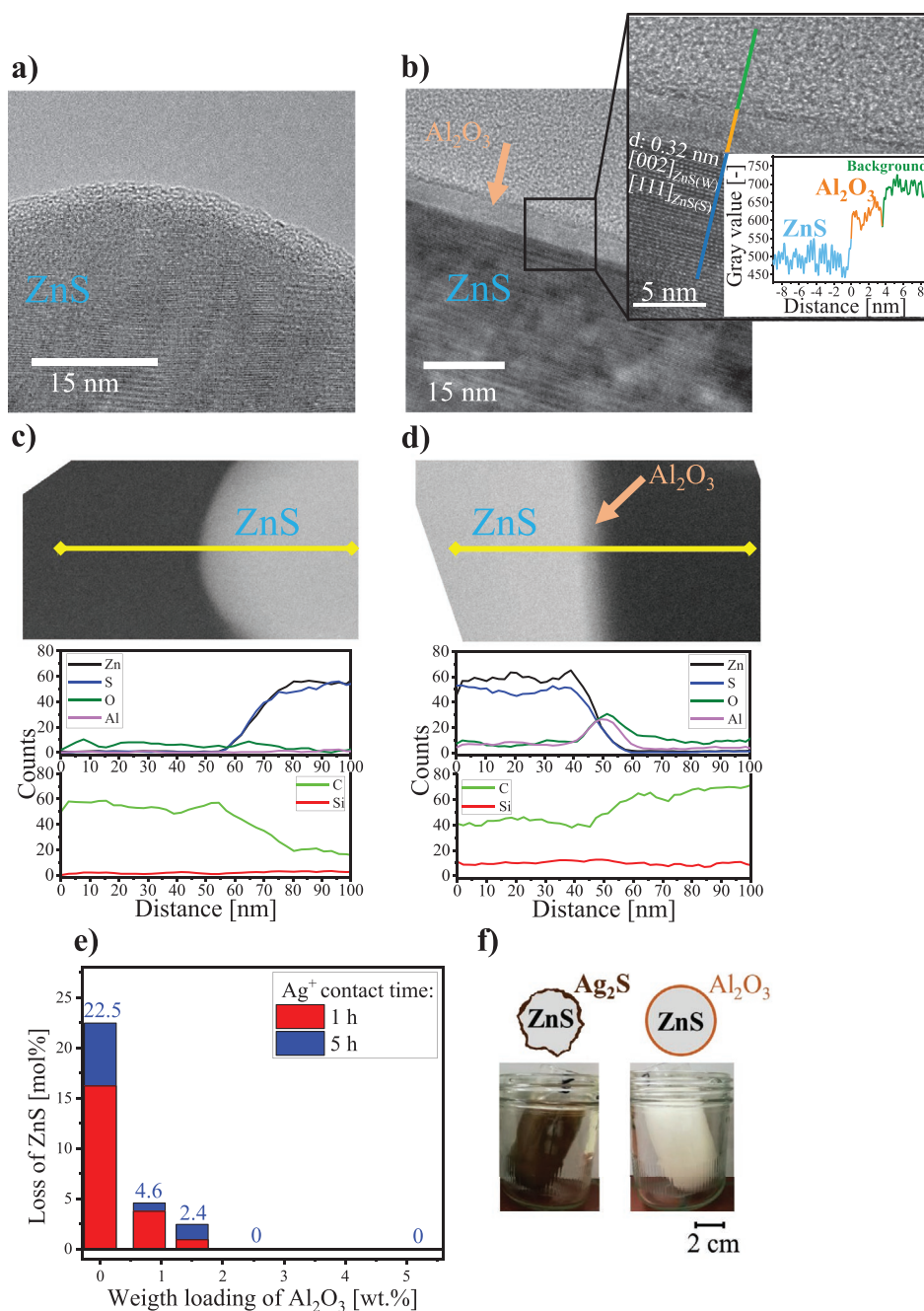


**Figure 3.** ALD layer characterization: TEM image of a FIB lamella cross-section of a) uncoated and b) coated ZnS (5.2 wt% Al<sub>2</sub>O<sub>3</sub>). The Inset in (b) shows an HR-TEM image with a line plot of the gray value to illustrate the thickness of the Al<sub>2</sub>O<sub>3</sub> layer. Based on the line plot of the gray value, a lattice spacing of  $d = 0.32$  nm was determined, which corresponds to the [002] and [111] plane of wurtzite (ZnS(W)) and sphalerite (ZnS(S)), respectively. EDX line scan of the FIB lamella cross-section of c) uncoated and d) coated ZnS (5.2 wt% Al<sub>2</sub>O<sub>3</sub>). Loss of ZnS after exposure to Ag<sup>+</sup> ions for 1 and 5 h as a function of e) the Al<sub>2</sub>O<sub>3</sub> weight loading. Pictures show Ag<sup>+</sup>-containing dispersions of uncoated (left) and coated (right) ZnS (5.2 wt% Al<sub>2</sub>O<sub>3</sub>) after f) 1 h.

required Al mass load to prevent photocorrosion (see Figure 2). Consequently, it can be concluded that all ZnS particles were completely coated with a dense protection layer during the ALD process, successfully preventing the ZnS surface from contact with H<sub>2</sub>O and Ag<sup>+</sup>. Thus, in contrast to the stabilization of sulfide nanoparticles, which were spin-coated as films on flat substrates before the Al<sub>2</sub>O<sub>3</sub> deposition,<sup>[12,18a,b]</sup> a

sophisticated 3D coating of all individual ZnS particles was achieved by rotary ALD.

To gain representative insight whether Al<sub>2</sub>O<sub>3</sub>, Al(OH)<sub>3</sub>, or Al(OH)<sub>3</sub> layers were formed during ALD, XPS measurements were performed with three identically produced ZnS@Al<sub>2</sub>O<sub>3</sub> samples (ZnS@Al<sub>2</sub>O<sub>3</sub> 1–3, each with 1.4 wt% Al  $\hat{=}$  2.6 wt% Al<sub>2</sub>O<sub>3</sub>). The XPS results of the O 1s and Al 2p line are exemplarily shown

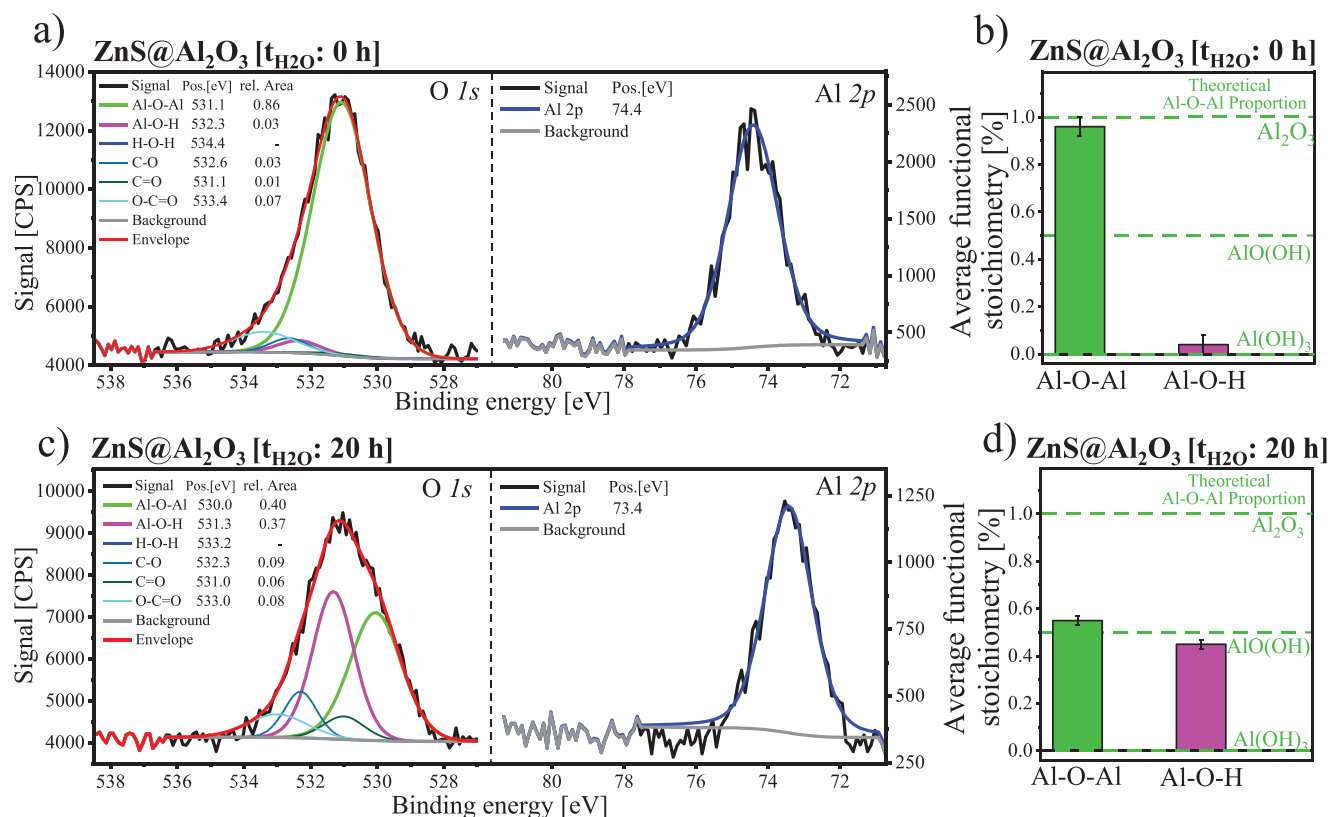


**Figure 4.** Protection layer's composition: a) O 1s and Al 2p peak and b) average functional stoichiometry of coated ZnS (ZnS-ALD-1; 2.6 wt% Al<sub>2</sub>O<sub>3</sub>). c) O 1s and Al 2p peak and d) average functional stoichiometry of coated ZnS after storage in H<sub>2</sub>O for 20 h (ZnS@Al<sub>2</sub>O<sub>3</sub>-1; 2.6 wt% Al<sub>2</sub>O<sub>3</sub>). The average functional stoichiometry was determined based on the relative areas of the Al-O-Al and Al-O-H curve fits (Tables 2 and 3).

for ZnS@Al<sub>2</sub>O<sub>3</sub>-1 in **Figure 4a**) (samples 2 and 3 are shown in Figure S4, Supporting Information). For the Al 2p peak, a deconvolution of the signal into contributions from aluminum oxyhydroxides, hydroxides, and oxides is very difficult since the respective peak positions differ by less than 0.5 eV.<sup>[36]</sup> In turn, the oxygen can be described by two distinct O 1s Al components namely Al-O-Al, present in Al<sub>2</sub>O<sub>3</sub> and AlO(OH), and Al-O-H, present in AlO(OH) and Al(OH)<sub>3</sub>, and a contribution from water (O<sub>H-O-H</sub>) located at 456.6 ± 0.1 eV, 458.0 ± 0.1 eV, and 460.2 ± 0.2 eV relative to the Al 2p line, respectively (fit see Figure 4a).<sup>[37]</sup> As the positions of the Al 2p and O 1s peak are not determined uniquely by charge correction with the C 1s peak, the O 1s components must be defined relative to the Al 2p line.<sup>[37,38]</sup> Additionally, O 1s peak contributions of C=O, C-O, and O-C=O, originating from carbonaceous contaminations, located at about 531.2,<sup>[39]</sup> 532.5,<sup>[39a]</sup> and 533.5 eV,<sup>[39b,40]</sup> respectively, were also considered by calculating the

theoretical peak area of each component according to the deconvolution of the C 1s line (see Figure S5, Supporting Information). Based on the relative areas of the Al-O-Al and Al-O-H curve fits, summarized in **Table 2**, the average functional stoichiometry of the deposited layer was calculated.

According to the result, the average functional stoichiometry of the deposited layer is found as (Al-O-Al)<sub>0.96±0.04</sub>(Al-O-H)<sub>0.04±0.04</sub> (see Figure 4b), which corresponds to Al<sub>2</sub>O<sub>3</sub> with about 4 ± 4% of hydrolyzed oxygen atoms. Furthermore, the XRD measurement after ALD treatment shows no additional diffraction peaks, indicating the presence of an amorphous Al<sub>2</sub>O<sub>3</sub> layer (see Figure S6, Supporting Information; diffraction peaks at 25.8° and 42.7°, which are already present in neat ZnS, most likely originate from PbS impurities in the industrial product<sup>[41]</sup>). The formation of Al<sub>2</sub>O<sub>3</sub> from TMA and H<sub>2</sub>O has been frequently confirmed on various surfaces based

**Table 2.** Relative area and separation from the Al 2p peak position of the Al-O-Al and Al-O-H curve fits, determined for samples ZnS-ALD 1-3 (each with 2.6 wt% Al<sub>2</sub>O<sub>3</sub>).

Sample	Al-O-Al			Al-O-H		
	Rel. Area (O 1s)	Distance to Al2p [eV]	Stoichiometric proportion	Rel. Area (O 1s)	Distance to Al2p [eV]	Stoichiometric proportion
ZnS@Al <sub>2</sub> O <sub>3</sub> -1	0.86	456.7	0.97	0.03	457.9	0.03
ZnS@Al <sub>2</sub> O <sub>3</sub> -2	0.86	456.6	1.00	0.00	457.9	0.00
ZnS@Al <sub>2</sub> O <sub>3</sub> -3	0.91	456.7	0.92	0.08	457.9	0.08

The stoichiometric proportion of Al-O-Al and Al-O-H was determined based on the relative peak areas.

on Rutherford backscattering<sup>[16c,28b,32a]</sup> and XPS,<sup>[42]</sup> while as-prepared layers are found to be amorphous<sup>[28b,32a,43]</sup>, which is consistent with our results. FTIR measurements performed during the ALD of Al<sub>2</sub>O<sub>3</sub> also revealed the presence of unreactive hydroxyls on the surface,<sup>[28c]</sup> which is in line with the proposed presence of hydroxide species following our XPS study.

### 2.3. Durability of the Protection Layer

Since ZnS is exposed to humid air or water when used, for example, as a photocatalyst, white pigment, polymer additive, or as component for optoelectronic devices, ZnS protected by a 1.6-nm-thick Al<sub>2</sub>O<sub>3</sub> layer (2.6 wt% Al<sub>2</sub>O<sub>3</sub>) was stored in water under constant stirring and the photostability was investigated by PL measurements for different H<sub>2</sub>O exposure times (see Figure 5a). As can be seen, the photostability shows no change during the first 5 h but starts to decrease after about 6 h of storage in H<sub>2</sub>O. After 10 h, the coated ZnS suffers significantly from photocorrosion and only 25% of the initial PL intensity remains after 40 min of UV illumination. This observation is independent of the layer thickness such that neither a 1.6 nm nor a 3.4 nm thick Al<sub>2</sub>O<sub>3</sub> layer provides a long-term protection (>20 h) against photocorrosion when stored in H<sub>2</sub>O (see Figure 5b). The

leaching of ZnS with AgNO<sub>3</sub> after storage for 1, 5, and 20 h in H<sub>2</sub>O again show very similar results to the photocorrosion test (Figure 5c) such that storage for more than 5 h in H<sub>2</sub>O leads to the onset of dissolving ZnS indicating that the protective Al<sub>2</sub>O<sub>3</sub> layer was perforated. Consequently, it is not sufficient to evaluate the success and durability of the surface passivation of an Al<sub>2</sub>O<sub>3</sub>-coated sulfide only by an UV illumination for about 20 min in ambient air, as performed by Cheng et al.<sup>[12]</sup>

XPS results of coated ZnS after exposure to H<sub>2</sub>O for 20 h (compare Figure 4a–c) show a significant peak shift of the O 1s to higher binding energies with respect to the Al 2p peak. Peak deconvolution of the O 1s line reveals that the average functional stoichiometry of the layer drastically changed from (Al-O-Al)<sub>0.96±0.04</sub>(Al-O-H)<sub>0.04±0.04</sub> to (Al-O-Al)<sub>0.55±0.02</sub>(Al-O-H)<sub>0.45±0.02</sub> during storage in water, which is in good agreement with the theoretical functional stoichiometry of AlO(OH) (see Figure 4d and Table 3—XPS spectra of samples 2 and 3 are given in Figure S7, Supporting Information). This hydrolysis of as-prepared Al<sub>2</sub>O<sub>3</sub> to AlO(OH) (R5) upon prolonged exposure to H<sub>2</sub>O is in line with the literature and was also observed by Ruckerl et al. during FTIR and grazing incidence XRD measurements.<sup>[21a]</sup> As this process is accompanied by a complete rearrangement of the surface and a significant increase in its roughness<sup>[21a]</sup>, and an AlO(OH) layer is about 36% less dense

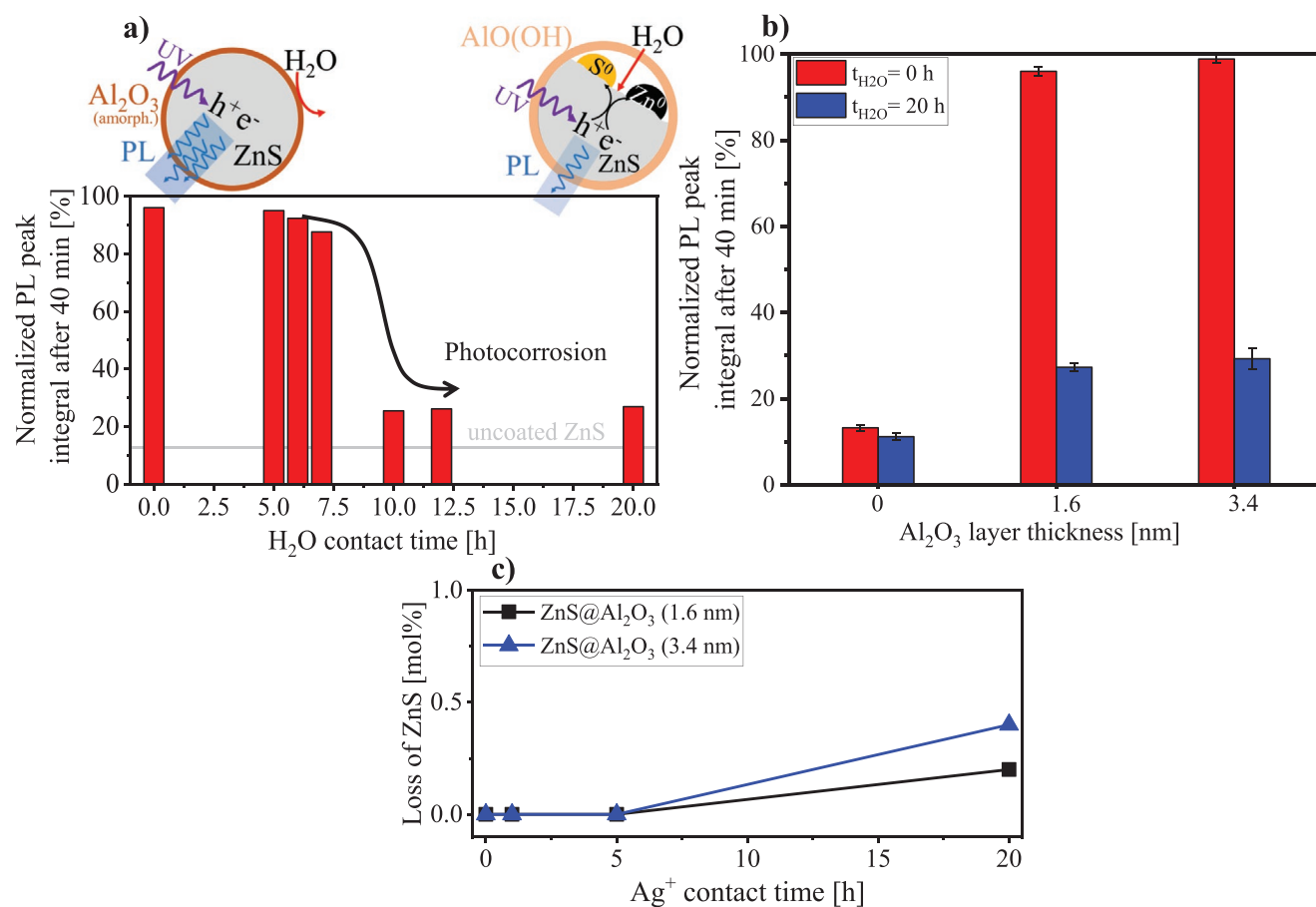


**Figure 5.** Wet photocorrosion: a) Normalized PL peak integral after 40 min of UV illumination as a function of the H<sub>2</sub>O contact time of ZnS@Al<sub>2</sub>O<sub>3</sub> (with 2.6 wt% Al<sub>2</sub>O<sub>3</sub>  $\hat{=}$  1.6 nm layer thickness). b) Normalized PL peak integral after storage in H<sub>2</sub>O for 20 h and 40 min of UV illumination for ZnS@Al<sub>2</sub>O<sub>3</sub> with various layer thicknesses. c) Loss of ZnS as a function of the contact time to Ag<sup>+</sup> ions.

**Table 3.** Relative area and separation from the Al 2p peak position of the Al-O-Al and Al-O-H curve fits, determined for samples ZnS-ALD 1-3 after storage in H<sub>2</sub>O for 20 h (each with 2.6 wt% Al<sub>2</sub>O<sub>3</sub>).

Sample	Al-O-Al			Al-O-H		
	Rel. Area (O 1s)	Distance to Al2p [eV]	Stoichiometric proportion	Rel. Area (O 1s)	Distance to Al2p [eV]	Stoichiometric proportion
ZnS@Al <sub>2</sub> O <sub>3</sub> -1	0.40	456.6	0.53	0.36	457.9	0.47
ZnS@Al <sub>2</sub> O <sub>3</sub> -2	0.42	456.7	0.55	0.34	457.8	0.45
ZnS@Al <sub>2</sub> O <sub>3</sub> -3	0.48	456.6	0.57	0.36	457.8	0.43

The stoichiometric proportion of Al-O-Al and Al-O-H was determined based on the relative peak areas.

compared to Al<sub>2</sub>O<sub>3</sub> produced by ALD (for the same amount of Al; calculated based on the densities  $\rho_{\text{Al}_2\text{O}_3} = 3.5 \text{ g cm}^{-3}$ <sup>[28a,b,31]</sup> and  $\rho_{\text{AlO(OH)}} = 3.02 \text{ g cm}^{-3}$ <sup>[44]</sup>), the hydrolysis of Al<sub>2</sub>O<sub>3</sub> to AlO(OH) presumably leads to the insufficient protection of the ZnS surface shown in Figure 5.



Due to the long-term hydrolysis susceptibility of the protective layers, ZnS@Al<sub>2</sub>O<sub>3</sub> (2.6 wt% Al<sub>2</sub>O<sub>3</sub>; 1.6-nm-thick layer) was calcined between 500 and 1000 °C, since a high-temperature treatment was already found to inhibit a water-induced increase in the thickness and roughness of as-prepared Al<sub>2</sub>O<sub>3</sub> layers.<sup>[45]</sup> PL intensity measurements before and after 20 h of storage in H<sub>2</sub>O shown in Figure 6a) reveal that the storage stability of the Al<sub>2</sub>O<sub>3</sub> coated ZnS was improved with increasing calcination temperature, with calcination at 800 °C and above showing the best stability results. Here, two effects appear to take place: the photostability before storage in water H<sub>2</sub>O for 20 h is slightly reduced, but the resistance to H<sub>2</sub>O increases significantly. Consequently, the calcined layer appears to be inert, but no longer completely covers the surface. Based on the O 1s and Al 2p peaks (see Figure S8 and Table S4, Supporting Information), the relative functional stoichiometry before and after exposure to water of the sample calcined at 1000 °C was determined (Figure 6b). Before storage in water, the non-calcined and calcined samples have a similar Al-O-Al proportion of about 95%, which corresponds to Al<sub>2</sub>O<sub>3</sub> with about 5% hydrolyzed oxygen atoms. However, in contrast to non-calcined ZnS@Al<sub>2</sub>O<sub>3</sub>, the calcined sample exhibits no change in the relative functional stoichiometry after prolonged storage in water, which reveals a successful prevention from hydrolysis to AlO(OH). Furthermore, XRD results show the presence of additional diffraction peaks at 37.7°, 45.7°, and 66.7° after calcination at 1000 °C (see Figure 6c), which can be assigned to the  $\gamma$ -Al<sub>2</sub>O<sub>3</sub> phase (ICSD card 039014). Thus, it can be concluded that the transformation from an amorphous to a crystalline  $\gamma$ -Al<sub>2</sub>O<sub>3</sub> layer is responsible for the higher resistance to water of the calcined samples. The crystallization of deposited Al<sub>2</sub>O<sub>3</sub> above 900 °C is accompanied by a shrinkage of the layer thickness, as previously shown in the literature.<sup>[43]</sup> This shrinkage is likely to have led to the decreased photocorrosion stability of the samples calcined at 900 and 1000 °C (see Figure 6a) due to an incomplete coverage of the ZnS surface. To compensate for this calcination-related volume reduction, ZnS@Al<sub>2</sub>O<sub>3</sub> with 5.2 wt% Al<sub>2</sub>O<sub>3</sub> (3.4-nm-thick layer) was also calcined at 1000 °C and investigated regarding its photostability before and after prolonged storage in H<sub>2</sub>O. Figure 6d shows that the calcination of ZnS coated with a thicker alumina layer

does not lead to a decrease in the photostability, nor does the subsequent storage in H<sub>2</sub>O. HR-TEM investigations of a FIB lamella cross-section of the calcined ZnS@ $\gamma$ -Al<sub>2</sub>O<sub>3</sub> particles reveal a layer thickness of about 2.9 nm (see Figure 6e). Thus, the protection layer indeed shrunk by approximately 15% during the calcination step (3.4 nm before calcination; see Figure 3b), in line with previous reports.<sup>[43]</sup> Furthermore, the gray value plot across the surface cross-section gives a lattice spacing of  $4.7 \pm 0.1 \text{ \AA}$  for the alumina layer (green), which is in good agreement with the [111]-lattice spacing of 4.6 Å for  $\gamma$ -Al<sub>2</sub>O<sub>3</sub><sup>[46]</sup> and in accordance with the presence of  $\gamma$ -Al<sub>2</sub>O<sub>3</sub> observed by XRD. The lattice spacing of  $2.9 \pm 0.2 \text{ \AA}$  of the underlying ZnS (blue) is in good agreement with the reported value of about 0.31 Å for the [002] or [111] plane of hexagonal wurtzite or cubic sphalerite, respectively,<sup>[33,34]</sup> and significantly differs from the determined lattice spacing of the  $\gamma$ -Al<sub>2</sub>O<sub>3</sub> phase. Between the crystalline ZnS and  $\gamma$ -Al<sub>2</sub>O<sub>3</sub> phase, only a very narrow transition area of about 0.8 nm is present (magenta), which shows a distance of about 4.2 Å to adjacent crystal planes. Thus, a significant formation of a ternary compound during calcination does not seem to occur during calcination.

Consequently, applying a 3.4-nm-thick amorphous Al<sub>2</sub>O<sub>3</sub> layer successfully counteracted the calcination-related layer shrinkage, which enabled the formation of a dense, inert, and crystalline  $\gamma$ -Al<sub>2</sub>O<sub>3</sub> layer that completely covers and protects the ZnS particles. In contrast to R uckerl et al., who prevented the degradation of as-prepared ALD-Al<sub>2</sub>O<sub>3</sub> to AlO(OH) by the subsequent deposition of a SiO<sub>2</sub> capping using molecular beam epitaxy,<sup>[21a]</sup> we showed that this hydrolysis can also be avoided by a calcination of the as-prepared amorphous Al<sub>2</sub>O<sub>3</sub> layer.

To investigate the long-term stability of ZnS particles with a 2.9-nm-thick  $\gamma$ -Al<sub>2</sub>O<sub>3</sub> layer under continuous excitation, the UV irradiation time during the PL measurements was extended from 40 min to 24 h. Here, the normalized PL peak integral shows no decrease after 24 h, revealing excellent long-term stability (see Figure S9, Supporting Information). Furthermore, the photostability was investigated under high peak power UV illumination using a pulsed 355-nm nanosecond laser with a maximum peak power density of 10.5 kW cm<sup>-2</sup>. PL spectra were recorded before and after irradiation for 3, 6, 10, and 16 s to evaluate the extent of photocorrosion. During the high-intensity UV laser irradiation, bare ZnS, ZnS@Al<sub>2</sub>O<sub>3</sub> (non-calcined), and ZnS@ $\gamma$ -Al<sub>2</sub>O<sub>3</sub> (calcined) show a very bright blue luminescence, which is illustrated in Figure 7b). Bare ZnS significantly suffers from photocorrosive Zn<sup>0</sup> formation under the high power illumination (Figure 7b) and shows a significant PL intensity loss of about 75% and 97% after 3 and 16 s, respectively (a). In contrast, the PL intensity of the non-calcined and calcined



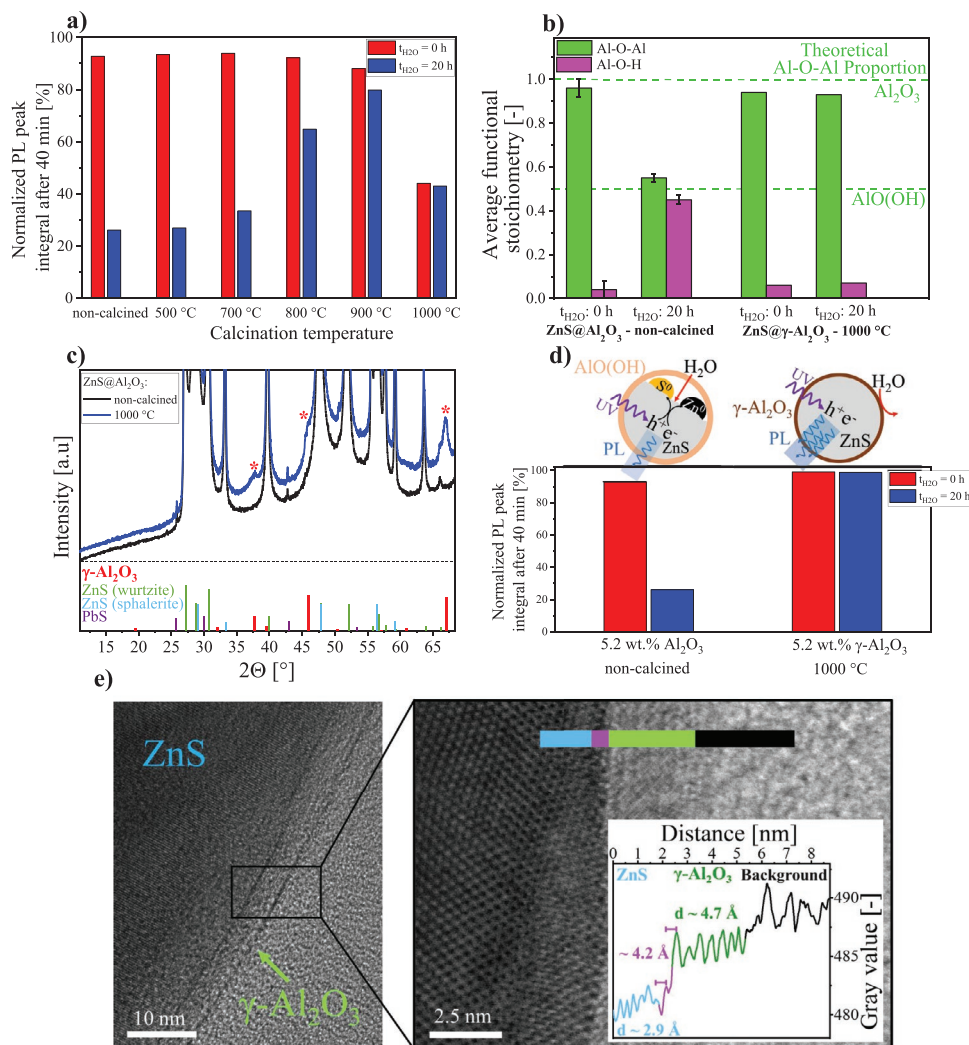


**Figure 6.** Durability and calcination of the layer: a) Normalized PL peak integral after 40 min of UV illumination before and after storage in H<sub>2</sub>O of ZnS@Al<sub>2</sub>O<sub>3</sub> (2.6 wt% Al<sub>2</sub>O<sub>3</sub>) calcined at different temperatures. b) Relative functional stoichiometry of (non)calcined ZnS@Al<sub>2</sub>O<sub>3</sub> (2.6 wt% Al<sub>2</sub>O<sub>3</sub>) before and after storage in H<sub>2</sub>O for 20 h. c) XRD pattern of (non-)calcined ZnS@Al<sub>2</sub>O<sub>3</sub> with reference data for  $\gamma$ -Al<sub>2</sub>O<sub>3</sub> (ICSD card 039014), ZnS wurtzite (JCPDS card 01-075-1534), ZnS sphalerite (JCPDS card 00-003-0579), and PbS precipitated in excess of S<sup>2-</sup> ions. Reproduced with permission.<sup>[41]</sup> Copyright 1991, Royal Society of Chemistry. The maxima of the patterns have been cut off to better display the reflection peaks of the  $\gamma$ -Al<sub>2</sub>O<sub>3</sub> phase. d) Normalized PL peak integral after 40 min of UV illumination before and after storage in H<sub>2</sub>O of (non-)calcined ZnS@Al<sub>2</sub>O<sub>3</sub> (5.2 wt% Al<sub>2</sub>O<sub>3</sub>). e) TEM image of a FIB lamella cross-section of ZnS@ $\gamma$ -Al<sub>2</sub>O<sub>3</sub> (5.2 wt% Al<sub>2</sub>O<sub>3</sub>) calcined at 1000 °C. The inset shows an HR-TEM image with a line plot of the gray value, which reveals a lattice spacing of 2.9 ± 0.2 and 4.7 ± 0.1 Å for the ZnS (blue) and  $\gamma$ -Al<sub>2</sub>O<sub>3</sub> phase (green), respectively. The transition area (magenta) shows a distance of about 4.2 Å to adjacent planes.

alumina-protected ZnS is maintained during the UV laser irradiation and the illuminated areas remain white (Figure 7b). Thus, the alumina coatings successfully protect the ZnS particles even under a high power UV laser irradiation with a peak power of 10.5 kW cm<sup>-2</sup>. Consequently, the presented data clearly reveal the high durability of the alumina coating, which ensures successful surface passivation even under humid conditions and long-term or high power UV irradiation.

#### 2.4. Influence of the Passivation Layer on Photophysical Properties

To determine whether the 3-nm-thick alumina layer influences the optical properties compared to pure ZnS particles, optical

absorption and time-resolved photoluminescence (TRPL) spectroscopy were performed. The absorption spectra of pure ZnS and ZnS@Al<sub>2</sub>O<sub>3</sub>, before and after the calcination step, respectively, are shown in Figure S10, Supporting Information. The shape of the spectra of calcined and non-calcined ZnS with and without Al<sub>2</sub>O<sub>3</sub> layer is very similar. All samples show a sharp absorption edge at around ≈3.5 eV. Due to the particle size of about 500 nm, the absorption spectra show a background originating from Mie scattering. An influence of the thin Al<sub>2</sub>O<sub>3</sub> layer on the absorption properties of ZnS particles cannot be detected.

Emissive states in ZnS and ZnS with Al<sub>2</sub>O<sub>3</sub> layer were investigated via TRPL spectroscopy. Figure 8 shows the TRPL decays of calcined and non-calcined ZnS with and without Al<sub>2</sub>O<sub>3</sub> layer.

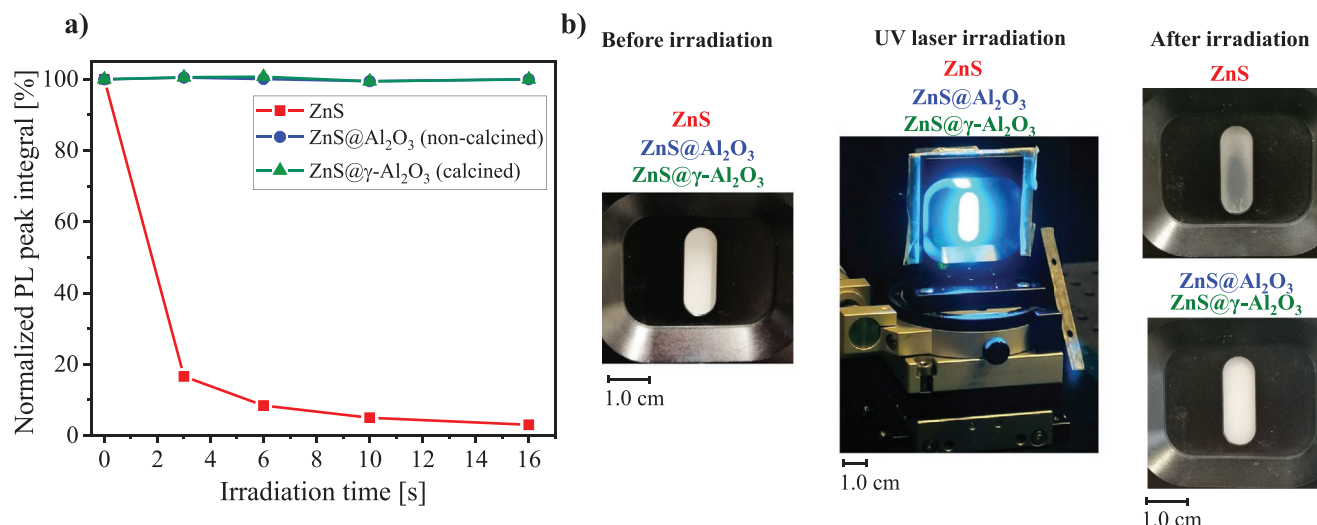


**Figure 7.** a) Corrosion resistance under high power irradiation: Normalized PL peak integral of ZnS and (non-)calcined ZnS@Al<sub>2</sub>O<sub>3</sub> (5.2 wt% Al<sub>2</sub>O<sub>3</sub>) after UV irradiation with a pulsed 355-nm nanosecond laser as a function of the illumination time (peak power density of the laser: 10.5 kW cm<sup>-2</sup>). b) Exemplary images before, during, and after the UV irradiation.

PL spectra show no shift in energy and no decrease in intensity when comparing bare ZnS particles and ZnS particles covered by an Al<sub>2</sub>O<sub>3</sub> layer (Figure 1a,b). TRPL reveals very similar PL decays for as-prepared non-calcined ZnS and ZnS@Al<sub>2</sub>O<sub>3</sub> as well as for the calcined ZnS and ZnS@γ-Al<sub>2</sub>O<sub>3</sub> (Figure 8a). The TRPL decays show two different lifetimes: a short lifetime

(≈μs) and a long lifetime component (≈ms). For both radiative centers (SA and B–Cu; most likely originating from chloride and/or copper impurities of the industrially produced ZnS<sup>[24]</sup>), lifetimes in the μs-regime have been reported,<sup>[47]</sup> in good agreement with the short lifetime component measured in this work. Due to electron traps that draw electrons from the

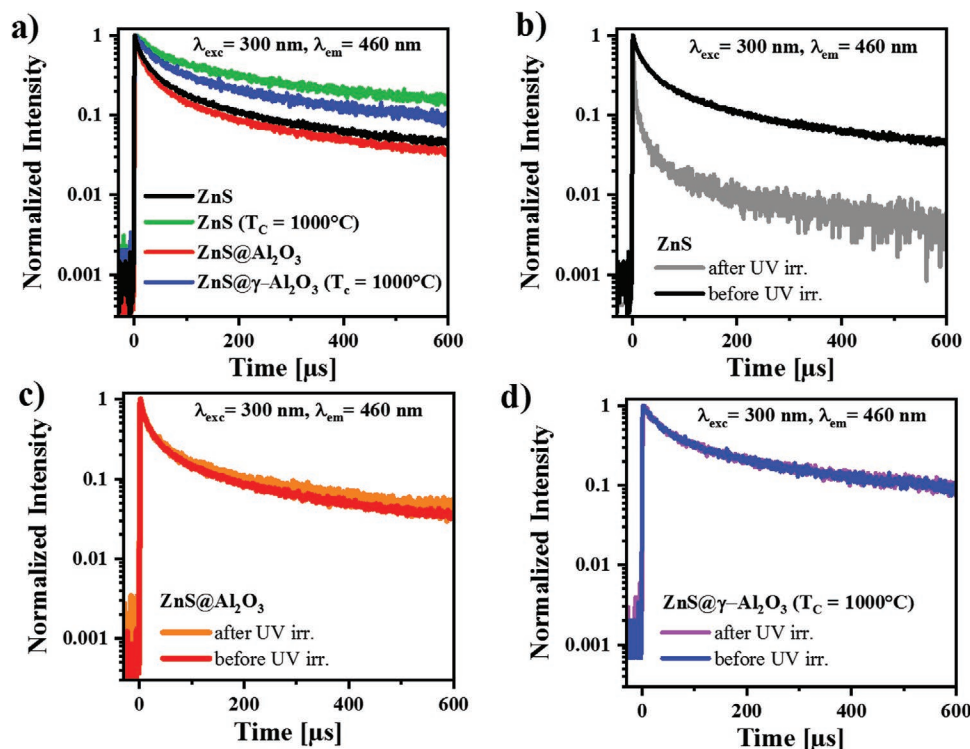


**Figure 8.** Influence on photophysical properties: a) TRPL decay curves of as-prepared ZnS (black), calcined ZnS (green), ZnS with an Al<sub>2</sub>O<sub>3</sub> layer (red), and calcined ZnS particles with a γ-Al<sub>2</sub>O<sub>3</sub> layer (blue). b–d) TRPL decay curves before and after 40 min UV irradiation of ZnS (black and grey), ZnS with an Al<sub>2</sub>O<sub>3</sub> layer (red and orange), and calcined ZnS particles with a γ-Al<sub>2</sub>O<sub>3</sub> layer (blue and purple) (UV irradiation parameter: λ = 330 nm; power density S = 14 mW cm<sup>-2</sup>).

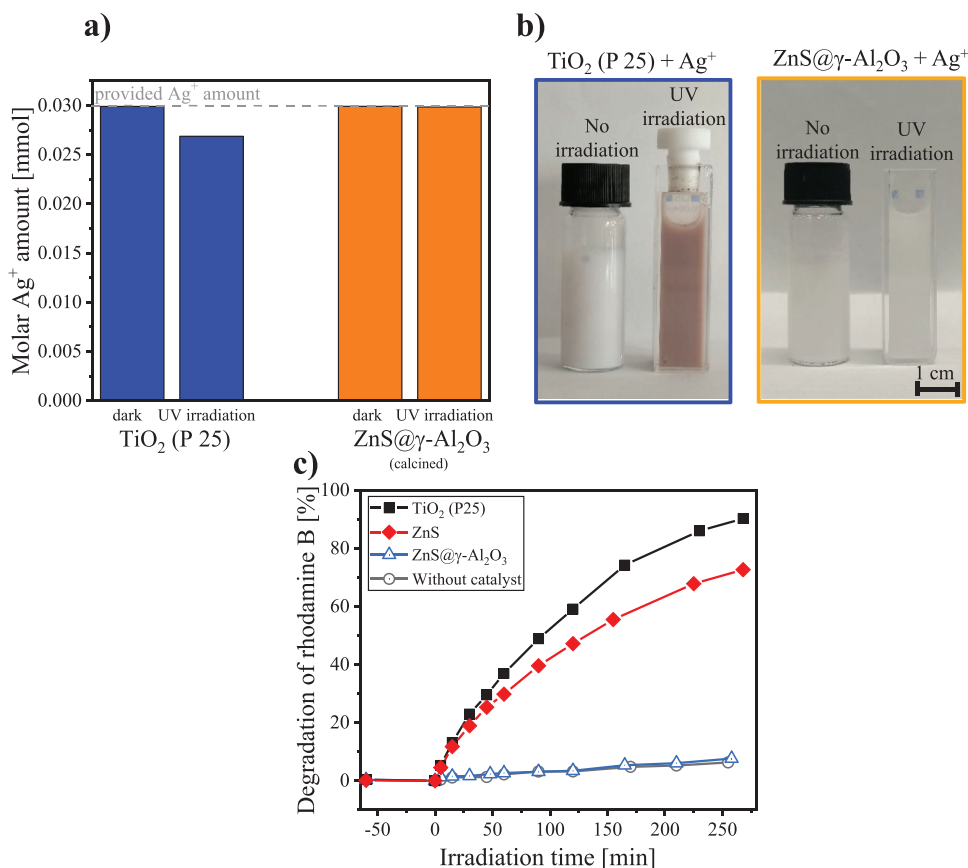


**Figure 9.** Charge carrier transport through the protection layer: a) Molar  $\text{Ag}^+$  amount and b) photographic images of  $\text{AgNO}_3$  dispersions containing  $\text{TiO}_2$  and  $\text{ZnS}@ \gamma\text{-Al}_2\text{O}_3$  (5.2 wt%) stirred with and without UV illumination for 60 min (UV irradiation parameter:  $\lambda = 330 \pm 2$  nm; power density  $S = 5$  mW  $\text{cm}^{-2}$ ). c) Photo-induced degradation of rhodamine B in the presence of  $\text{TiO}_2$  (P 25), ZnS, and  $\text{ZnS}@ \gamma\text{-Al}_2\text{O}_3$  as well as in the absence of a photocatalyst.

vicinity of the excited centers, for example, Zn vacancies or Cu interstitials, a long lifetime component is reported for ZnS as well.<sup>[48]</sup> The non-calcined samples show a more pronounced short lifetime, possibly due to the healing of these electron-trapping defects by calcination. Additionally, TRPL measurements were conducted after 40 min of UV irradiation at  $\lambda = 330$  nm (Figure 8b–d). The TRPL decay of pure ZnS particles drastically changes after UV irradiation, which can be attributed to the photocorrosion of the non-protected ZnS surface (b). While the long lifetime component—most likely controlled by the presence of electron trap states<sup>[48a]</sup>—is barely affected, the short decay component becomes much more prominent, indicating enhanced loss channels after the occurrence of photocorrosion. In contrast, the decay curves of alumina-protected ZnS remain the same after UV irradiation, which can be attributed to the passivation of the surface and suppression of photocorrosion. Consequently, the absorption and TRPL spectroscopy investigations validate that the  $\text{Al}_2\text{O}_3$  protection layer does not affect the optical properties of ZnS particles, but maintains them even under prolonged UV irradiation.

## 2.5. Transport of Charge Carriers through the Alumina Layer

For a qualitative evaluation, if photogenerated electrons can pass the protection layer or not, the reduction of  $\text{Ag}^+$  ions was

performed under UV illumination and compared to  $\text{TiO}_2$  (P 25) as typical photoactive reference material. The photoreduction of  $\text{Ag}^+$  to  $\text{Ag}^0$  by photogenerated electrons is a common method in the literature to deposit  $\text{Ag}^0$  onto semiconductor surfaces.<sup>[49]</sup> To investigate the reduction of  $\text{Ag}^+$  ions, particle suspensions of ZnS (or  $\text{TiO}_2$ ) containing 0.01 M  $\text{AgNO}_3$  were irradiated for 60 min with UV light and subsequently analyzed for the remaining  $\text{Ag}^+$  ion amount. The UV irradiation of the  $\text{TiO}_2$  suspension led to a photodeposition of brownish  $\text{Ag}^0$ , which is in line with previous observations,<sup>[50]</sup> and was accompanied by a decrease of the  $\text{Ag}^+$  ions of about 10 mol% (see Figure 9a,b). In turn, an identical suspension that was stored in the dark for 60 min as a reference sample did not show any  $\text{Ag}^0$ -related discoloration nor change in the concentration of  $\text{Ag}^+$  ions. When testing the ZnS coated with a 2.9-nm-thick  $\gamma\text{-Al}_2\text{O}_3$  layer, neither discoloration nor consumption of  $\text{Ag}^+$  ions was observed after UV irradiation for 60 min. Since the reduction of the  $\text{Ag}^+$  ions did not take place during UV irradiation of  $\text{ZnS}@ \gamma\text{-Al}_2\text{O}_3$ , it can be concluded that the photoelectrons cannot pass the protective layer under the prevailing conditions.

To investigate the transport of photogenerated holes through the layer, the oxidative decomposition of an organic dye (rhodamine B) was performed with coated and uncoated ZnS, which is a common model experiment for the degradation of pollutants.<sup>[51]</sup> Figure 9c) shows the degradation of rhodamine B under UV irradiation in the presence (and absence)

of ZnS, ZnS@ $\gamma$ -Al<sub>2</sub>O<sub>3</sub>, and P 25 (TiO<sub>2</sub> as literature reference). Before the illumination, each suspension was stored for 60 min in the dark to exclude adsorption effects. In line with previous works,<sup>[51,52]</sup> TiO<sub>2</sub> and ZnS show significant activity in the dye decomposition, with degradation of rhodamine B of about 90% and 70% after 270 min, respectively. However, a sulfate quantification of the ZnS suspension after the irradiation by ion chromatography revealed the formation of 0.5 mmol sulfate, which corresponds to a photocorrosive dissolution of ZnS of about 25 mol%. Thus, the degradation of rhodamine B by ZnS was accompanied by a significant extent of photocorrosion. ZnS@ $\gamma$ -Al<sub>2</sub>O<sub>3</sub> shows no degradation of rhodamine B compared to the blind test without a photocatalyst (Figure 9c) and did not suffer from photocorrosive dissolution. Thus, direct oxidation of rhodamine B by photo-generated holes did not occur, which can be attributed to a lack of hole transport through the protection layer. Consequently, the photoreduction and dye degradation experiments revealed that both, the photogenerated electrons and holes, are not able to pass the 2.9-nm-thick  $\gamma$ -Al<sub>2</sub>O<sub>3</sub> protection layer under the prevailing conditions. Thus, for photocatalytic processes, further optimization of the protection layer regarding the minimum thickness should be considered, which possibly enables the transport of charge carriers. However, for optoelectronic applications such as high-field electroluminescent devices operated with alternating current, an insulating nature of the passivation layers enclosing the luminescent film and ensuring corrosion stability is required.

### 3. Conclusion

Within the class of metal sulfides, ZnS gained increasing attention in recent years due to its remarkable, easily tunable photophysical properties and shows high potential for various applications like semiconductor-based photocatalysis or optoelectronic devices such as FED and photodetectors. A drawback of ZnS, however, is its susceptibility towards charge carrier-induced oxidation in the presence of water/moisture, which can affect its long-term stability and requires sufficient surface passivation. We presented the ALD of a 3-nm-thick insulating alumina coating inside a spinning drum reactor that completely protected exceedingly photosensitive ZnS particles from self-decomposition even under high power and long-term UV irradiation by spatial separation of water and the particle surfaces, without altering the photophysical properties. The combination of HR-TEM investigations, PL and IR spectroscopy, EDX line scans, and the highly sensitive reaction between sulfide surfaces and Ag<sup>+</sup> ions clearly confirmed the formation of a dense Al<sub>2</sub>O<sub>3</sub> protection layer that completely covers all ZnS particles. Durability tests revealed that the hydrolysis of the as-prepared Al<sub>2</sub>O<sub>3</sub> coatings upon prolonged exposure to water enables the penetration of H<sub>2</sub>O and Ag<sup>+</sup> ions and causes an insufficient protection of the ZnS surface. To prevent this hydrolysis, a calcination step at 1000 °C can be applied after the ALD procedure, causing the crystallization of amorphous Al<sub>2</sub>O<sub>3</sub> to  $\gamma$ -Al<sub>2</sub>O<sub>3</sub>.

The presented scalable stabilization method is transferable to the whole class of oxidation-prone metal sulfides and

particularly promising for applications like optoelectronic devices (e.g., FED), pigments, or polymer additives, where (photo-)excited charge carriers and moisture/water will cause a corrosive degradation.

### 4. Experimental Section

**Atomic Layer Deposition:** Commercial mixed-phase zinc sulfide powder (Venator Germany GmbH,  $d_{50}$ : 570 nm; wurtzite:sphalerite ratio about 1:1) was coated using an ALD system (Savannah, Veeco). To coat the ZnS equally with an Al<sub>2</sub>O<sub>3</sub> protection layer, 2 g of the ZnS sub-microparticles were added to the rotary drum reactor as dry powder. The system was evacuated and the reactor chamber heated up to 150 °C. At a rotational speed of 4 rpm, the powder was first dried for 45 min at an argon flow of 20 sccm (standard cm<sup>3</sup> min<sup>-1</sup>). For the deposition of the protective Al<sub>2</sub>O<sub>3</sub> layer, trimethylaluminum (TMA, Sigma-Aldrich, 97%) and water were used as precursors at 25 °C and pulsed into the reactor following a predetermined procedure. First, TMA was pulsed by opening the valve of the TMA storage cylinder for 0.08 s (argon flow: 5 sccm) followed by a 40-sec waiting period and a 70-sec purge step. This sub-procedure was repeated 9 times and represents the TMA half cycle. After a 5-minute purge step with dry argon (20 sscm), water was dosed by opening the valve of the H<sub>2</sub>O storage cylinder for 0.25 s followed by a 10-sec waiting period and a 35-sec purge step. This sub-procedure was repeated 7 times and represents the H<sub>2</sub>O half cycle. Before the next TMA half cycle, a 5-minute purge step was performed. A detailed description of this sequence is given in Figure S11, Supporting Information. The calcination of coated samples was carried out under nitrogen atmosphere in a tube furnace (Carbolite). After mounting the sample, the furnace was flushed with nitrogen for 12 h, before the temperature was raised to the target value at a heating rate of 5 K min<sup>-1</sup> and held for 1 h.

**Photostability Measurements:** The photocorrosive zinc formation which is indicated by a decreased PL intensity<sup>[23,25]</sup> was analyzed with a fluorescence spectrometer (Fluorolog-3, HORIBA). 400 mg sample was intensively mixed with 200  $\mu$ L demineralized water, placed on the sample holder, and fixed with a quartz glass plate. The sample was then irradiated for 40.5 (or 90) min with an excitation wavelength of 330  $\pm$  2 nm (5 mW cm<sup>-2</sup>), whereby an emission spectrum from 350 to 650 nm (slit width to the detector 1 nm) was recorded every 90 s. By integrating the respective emission band and subsequent normalization to the initial integral, the relative temporal decrease of the PL intensity was determined. To investigate the photostability under high power UV irradiation, the samples were irradiated with a pulsed 355-nm laser (AVIA, Coherent) with a maximum peak power density of 10.5 kW cm<sup>-2</sup> and an average power density of 18 W cm<sup>-2</sup> (3rd harmonic of an Nd:YAG Laser; repetition rate: 50 kHz; fluence: 420  $\mu$ J cm<sup>-2</sup>; pulse length: 40 ns). Before and after the laser irradiation, an emission spectrum from 350 to 650 nm was recorded with the fluorescence spectrometer.

The photocorrosive sulfate formation was monitored by DRIFTS using an FT-IR spectrometer (iS50R, ThermoScientific), equipped with a Harrick HVC-DRP-5 in situ cell with temperature control. After sample insertion, the IR cell was flushed with moist He ( $\approx$ 6000 ppm H<sub>2</sub>O) at 20 mL min<sup>-1</sup> for 60 min. Afterward, UV light stemming from a 200 W Xe(Hg) lamp from Oriel was applied through a quartz glass window, while corresponding IR spectra were recorded after 15, 35, and 55 min of irradiation. Difference spectra were then generated using the IR spectra before and after the illumination to evaluate the change of the sulfate regime ( $\approx$ 1000–1300 cm<sup>-1</sup>).

**Layer Characterization:** To quantify the deposited Al amount, 300 mg sample was placed in a 250 mL two-neck flask and mixed with 100 mL 2 N HCl (Fluka Analytical, Reag. Ph. Eu.). The dispersion was then heated to 90 °C and stirred for 3 h to completely dissolve the sample. Meanwhile, the solution was continuously flushed with N<sub>2</sub> (2 L h<sup>-1</sup>) to expel the formed H<sub>2</sub>S. The clear solution was then analyzed for the aluminum concentration by ICP-MS.



To investigate if the ZnS surface was completely covered by a dense Al<sub>2</sub>O<sub>3</sub> protection layer, the formation of Ag<sub>2</sub>S in an AgNO<sub>3</sub> solution was used as an indicator if uncovered ZnS surface remained. 50 mg sample was added to 44 mL demineralized water, dispersed in an ultrasonic bath for 2 min, and mixed with 6 mL 0.1 M silver nitrate solution (Sigma-Aldrich, Reag. Ph. Eur.) while stirring. After 1, 5, and 20 h, the dispersion was centrifuged for 20 min at 5000 rpm, the clear supernatant was removed and the Ag<sup>+</sup> concentration of the supernatant was analyzed by ICP-MS. The relative loss of ZnS was then calculated via the Ag<sup>+</sup> concentration in the supernatant:

$$\text{Loss of ZnS [mol\%]} = \frac{n_0(\text{Ag}^+) - n_t(\text{Ag}^+)}{2 \times n(\text{ZnS})} \cdot 100\% \quad (2)$$

where  $n_0(\text{Ag}^+)$  is the initial amount of Ag<sup>+</sup> ions [mol],  $n_t(\text{Ag}^+)$  is the amount of Ag<sup>+</sup> ions after 1, 5, or 20 h [mol], and  $n(\text{ZnS})$  is the amount of ZnS [mol].

To investigate the thickness of the Al<sub>2</sub>O<sub>3</sub> protection layer on the nanoscopic scale, the particles were cut by FIB and the particle cross-section was investigated by HR-TEM and EDX. At first, the particles were placed on a Si wafer via drop-coating and stabilized by C and Pt sputtering. Afterward, two rectangular holes were drilled via FIB, leaving a thin lamella of cross-sectioned microparticles, which then was adhered to a microtip by Pt sputtering. Subsequently, the lamella was taken out by cutting it from the surrounding powder bed, adhered to a TEM grid, and thinned by FIB. The TEM grid was then transferred to a high-resolution transmission electron microscope (JEM 2200FS, JEOL) for analysis of the particle cross-sections.

XPS spectra of the samples were collected on a PHI VersaProbe II scanning X-ray photoelectron spectroscope using a monochromated Al K $\alpha$  X-ray source (1486.6 eV) with a pass energy of 23.5 eV. By applying an ion and flood gun, the charge neutralization was ensured. Analysis of the spectra was performed with the software CasaXPS, while all spectra were corrected using a C 1s peak shift to center at 284.8 eV.

XRD was carried out on a Panalytical MPD diffractometer operated at a voltage of 30 kV and a current of 10 mA with Cu K $\alpha$  radiation. The data were collected in the range of 10°–90° (2 $\theta$ ) with a step size of 0.02°.

To investigate the influence of the protection layer on the optical properties of the ZnS particles, absorption and TRPL spectroscopy were conducted. For optical absorption measurements, the samples were dispersed in de-ionized water (4.7 mg mL<sup>-1</sup>) and further diluted with de-ionized water to a ratio of 1:10. The diluted dispersion was measured using an UV–vis spectrophotometer with an integrating sphere (UV2550, Shimadzu).

TRPL was measured with time-correlated single photon counting (TCSPC) in a spectrofluorometer (Fluorolog-3 FL-1040, Horiba). The samples were dispersed in de-ionized water (4.7 mg mL<sup>-1</sup>) and multiple layers drop-casted on silicon substrates. A UV xenon flash lamp with a time resolution of  $\Delta t = 10 \mu\text{s}$  was used. Measurements were conducted in ambient atmosphere and carried out with an energy density of 0.2 nJ cm<sup>-2</sup>.

**Electron and Hole Transport through the Protection Layer:** For the photoreduction of Ag<sup>+</sup> ions, 75 mg sample was suspended in 3 mL 0.01 M silver nitrate solution (Sigma-Aldrich, Reag. Ph. Eur.) and dispersed in an ultrasonic bath for 2 min. The dispersion was UV irradiated at  $\lambda = 330 \pm 2 \text{ nm}$  (5 mW cm<sup>-2</sup>) for 60 min under constant stirring and then centrifuged at 15 000 rpm for 20 min. Subsequently, the Ag<sup>+</sup> concentration of the clear supernatant was determined by an UV–vis spectrometer (Evolution 201, Thermo Scientific) using the absorbance at 300 nm. TiO<sub>2</sub> (P 25; Evonik formerly Degussa) was used as a photoactive reference material for comparison with ZnS@ $\gamma$ -Al<sub>2</sub>O<sub>3</sub>.

To investigate the photo-induced degradation of rhodamine B, 200 mg sample was added to 200 mL 0.4  $\times 10^{-4}$  M rhodamine B solution (Sigma-Aldrich) and dispersed for 1 min in an ultrasonic bath. The dispersion was placed in a self-made quartz glass reactor, stored in the dark for 60 min, and then irradiated with a 200 W He(Hg) arc lamp under constant stirring.

At different points in time, a volume of about 1.5 mL was taken, centrifuged at 15 000 rpm for 10 min, and examined for the concentration of rhodamine B using UV–vis spectroscopy (Evolution 201, Thermo Scientific). After the irradiation, the ZnS-containing solutions were centrifuged and analyzed for sulfate content by ion chromatography (930 Compact IC, Metrohm).

## Supporting Information

Supporting Information is available from the Wiley Online Library or from the author.

## Acknowledgements

This work was funded by the Deutsche Forschungsgemeinschaft (DFG, German Research Foundation) – 388390466 – TRR 247.

Open access funding enabled and organized by Projekt DEAL.

## Conflict of Interest

The authors declare no conflict of interest.

## Data Availability Statement

The data that support the findings of this study are available from the corresponding author upon reasonable request.

## Keywords

alumina coatings, atomic layer deposition, corrosion, surface protection, zinc sulfides

Received: November 1, 2020

Revised: December 18, 2020

Published online:

- [1] a) S. Chandrasekaran, L. Yao, L. Deng, C. Bowen, Y. Zhang, S. Chen, Z. Lin, F. Peng, P. Zhang, *Chem. Soc. Rev.* **2019**, *48*, 4178; b) W. Choi, N. Choudhary, G. H. Han, J. Park, D. Akinwande, Y. H. Lee, *Mater. Today* **2017**, *20*, 116.
- [2] a) X. Fang, T. Zhai, U. K. Gautam, L. Li, L. Wu, Y. Bando, D. Golberg, *Prog. Nat. Sci.* **2011**, *56*, 175; b) G.-J. Lee, J. J. Wu, *Powder Technol.* **2017**, *318*, 8.
- [3] a) X. Xu, S. Li, J. Chen, S. Cai, Z. Long, X. Fang, *Adv. Funct. Mater.* **2018**, *28*, 1802029; b) X. Fang, L. Wu, L. Hu, *Adv. Mater.* **2011**, *23*, 585.
- [4] a) B. L. Abrams, L. Williams, J.-S. Bang, P. H. Holloway, *J. Electrochem. Soc.* **2003**, *150*, H105; b) P. H. Holloway, T. A. Trottier, J. Sebastian, S. Jones, X.-M. Zhang, J.-S. Bang, B. Abrams, W. J. Thomes, T.-J. Kim, *J. Appl. Phys.* **2000**, *88*, 483.
- [5] a) F. Liang, Y. Liu, Y. Hu, Y.-L. Shi, Y.-Q. Liu, Z.-K. Wang, X.-D. Wang, B.-Q. Sun, L.-S. Liao, *ACS Appl. Mater. Interfaces* **2016**, *9*, 20239; b) L. He, L. Yang, B. Liu, J. Zhang, C. Zhang, S. Liu, S. Chen, J. A. Zapien, K. A. Alamry, A. M. Asiri, K. Zhang, S. Wang, *J. Alloys Compd.* **2019**, *787*, 537; c) V. Lahariya, M. Ramrakhiani, *Luminescence* **2020**, *50*, 7602.

- [6] S. Ummartyotin, Y. Infahsaeng, *Renewable Sustainable Energy Rev.* **2016**, 55, 17.
- [7] a) W. Grassmann, *Farbe Lack* **1960**, 66, 67; b) M. Rohe, M. Kretschmer (Sachtleben Chemie GmbH), *Ger. DE102013105794A1*, **2015**.
- [8] a) S. David, S. Fritzen, L. Heiming (Sachtleben Chemie GmbH), *Ger. DE102007029070A1*, **2007**; b) T. Uhlenbroich, A. Djamschid (Metallgesellschaft AG), *Ger. EP0989160A1*, **2000**.
- [9] a) J. Cawley, *Chem. News J. Ind. Sci.* **1881**, 44, 51; b) A. Schleede, *Z. Phys. Chem.* **1923**, 106U, 386; c) P. Lenard, *Ann. Phys.* **1922**, 373, 553; d) Z. Morlin, *Phys. Status Solidi B* **1962**, 2, 205; e) P. Sviszt, *Phys. Status Solidi B* **1964**, 4, 631; f) P. Sviszt, P. Kovács, *Phys. Status Solidi B* **1965**, 9, K5; g) S. Shionoya, K. Watanabe, *BCSJ* **1957**, 30, 118; h) P. Weide, K. Schulz, S. Kaluza, M. Rohe, R. Beranek, M. Muhler, *Langmuir* **2016**, 12641; i) H. Platz, P. W. Schenk, *Angew. Chem., Int. Ed.* **1936**, 49, 822; j) P. W. Schenk, M. E. Schenk, *Z. Anorg. Chem.* **1947**, 255, 45.
- [10] a) D. Chen, F. Huang, G. Ren, D. Li, M. Zheng, Y. Wang, Z. Lin, *Nanoscale* **2010**, 2, 2062; b) J. F. Reber, K. Meier, *J. Phys. Chem.* **1984**, 88, 5903; c) M. Shamsipur, H. Reza Rajabi, O. Khani, *Mater. Sci. Semicond. Process.* **2013**, 16, 1154.
- [11] E. Becker, *Lithopone*, Berliner Union GmbH, Stuttgart, Germany **1957**.
- [12] C.-Y. Cheng, M.-H. Mao, *J. Appl. Phys.* **2016**, 120, 083103.
- [13] K. Gloor, *Helv. Chim. Acta* **1937**, 20, 853.
- [14] a) M. Muruganandham, A. Ramakrishnan, Y. Kusumoto, M. Sillanpaa, *Phys. Chem. Chem. Phys.* **2010**, 12, 14677; b) Y. Zhou, G. Chen, Y. Yu, Y. Feng, Y. Zheng, F. He, Z. Han, *Phys. Chem. Chem. Phys.* **2015**, 17, 1870.
- [15] M. L. Sall, A. K. D. Diaw, D. Gningue-Sall, S. Efremova Aaron, J.-J. Aaron, *Environ. Sci. Pollut. Res.* **2020**, 27, 29927.
- [16] a) R. L. Puurunen, *J. Appl. Phys.* **2005**, 97, 121301; b) S. M. George, *Chem. Rev.* **2010**, 110, 111; c) M. D. Groner, F. H. Fabreguette, J. W. Elam, S. M. George, *Chem. Mater.* **2004**, 16, 639; d) R. L. Puurunen, *Chem. Vap. Deposition* **2014**, 20, 332.
- [17] a) T. Suntola, J. Hyvarinen, *Annu. Rev. Mater. Sci.* **1985**, 15, 177; b) J. W. Lim, S. J. Yun, *Jpn. J. Appl. Phys.* **2003**, 42, L663; c) K. Vanbesien, P. de Visschere, P. F. Smet, D. Poelman, *Thin Solid Films* **2006**, 514, 323; d) T. Suntola, A. J. Pakkala, S. Lindfors, *US 4413022*, **1983**; e) M. Leskelä, M. Mattinen, M. Ritala, *J. Vac. Sci. Technol., B* **2019**, 37, 030801.
- [18] a) H.-M. So, H. Choi, H. C. Shim, S.-M. Lee, S. Jeong, W. S. Chang, *Appl. Phys. Lett.* **2015**, 106, 093507; b) C. Hu, A. Gassenq, Y. Justo, K. Devloo-Casier, H. Chen, C. Detavernier, Z. Hens, G. Roelkens, *Appl. Phys. Lett.* **2014**, 105, 171110; c) T. P. Brennan, O. Trejo, K. E. Roelofs, J. Xu, F. B. Prinz, S. F. Bent, *J. Mater. Chem. A* **2013**, 1, 7566; d) R. Ihly, J. Tolentino, Y. Liu, M. Gibbs, M. Law, *ACS Nano* **2011**, 5, 8175; e) R. Bose, A. Dangerfield, S. M. Rupich, T. Guo, Y. Zheng, S. Kwon, M. J. Kim, Y. N. Gartstein, A. Esteve, Y. J. Chabal, A. V. Malko, *ACS Appl. Nano Mater.* **2018**, 1, 6782; f) K. E. Roelofs, T. P. Brennan, J. C. Dominguez, C. D. Bailie, G. Y. Margulis, E. T. Hoke, M. D. McGehee, S. F. Bent, *J. Phys. Chem. C* **2013**, 117, 5584; g) N. Mahmoud, W. Walravens, J. Kuhs, C. Detavernier, Z. Hens, G. Roelkens, *ACS Appl. Nano Mater.* **2019**, 2, 299; h) M. Palei, V. Caligiuri, S. Kudara, R. Krahn, *ACS Appl. Mater. Interfaces* **2018**, 10, 22356.
- [19] A. Loiudice, S. Saris, E. Oveysi, D. T. L. Alexander, R. Buonsanti, *Angew. Chem., Int. Ed.* **2017**, 56, 10696.
- [20] D. Valdesueiro, M. K. Prabhu, C. Guerra-Nunez, C. S. S. Sandeep, S. Kinge, L. D. A. Siebbeles, L. C. P. M. de Smet, G. M. H. Meesters, M. T. Kreutzer, A. J. Houtepen, J. R. van Ommen, *J. Phys. Chem. C* **2016**, 120, 4266.
- [21] a) A. Rückerl, R. Zeisel, M. Mandl, I. Costina, T. Schroeder, M. H. Zoellner, *J. Appl. Phys.* **2017**, 121, 025306; b) B. Diaz, E. Härkönen, V. Maurice, J. Światowska, A. Seyeux, M. Ritala, P. Marcus, *Electrochim. Acta* **2011**, 56, 9609.
- [22] M. Liu, X. Xie, L. Chen, X. Wang, Y. Cheng, F. Lu, W.-H. Wang, J. Yang, X. Du, J. Zhu, H. Liu, H. Dong, W. Wang, H. Liu, *J. Mater. Sci. Technol.* **2016**, 32, 489.
- [23] S. Shionoya, in *Luminescence of Inorganic Solids* (Ed: P. Goldberg), Academic Press, Boston, MA **1966**, pp. 206–277.
- [24] M. Saleh, K. G. Lynn, L. G. Jacobsohn, J. S. McCloy, *J. Appl. Phys.* **2019**, 125, 075702.
- [25] P. Sviszt, *Phys. Status Solidi A* **1971**, 4, K113.
- [26] W. Hertl, *Langmuir* **1988**, 4, 594.
- [27] a) J. Marlowe, S. Acharya, A. Zuber, G. Tsilomelekis, *Catalysts* **2020**, 10, 726; b) K. Ben Mabrouk, T. H. Kauffmann, H. Aroui, M. D. Fontana, *J. Raman Spectrosc.* **2013**, 44, 1603.
- [28] a) A. W. Ott, J. W. Klaus, J. M. Johnson, S. M. George, *Thin Solid Films* **1997**, 292, 135; b) S. J. Yun, K.-H. Lee, J. Skarp, H.-R. Kim, K.-S. Nam, *J. Vac. Sci. Technol., A* **1997**, 15, 2993; c) A. C. Dillon, A. W. Ott, J. D. Way, S. M. George, *Surf. Sci.* **1995**, 322, 230.
- [29] M. M. Sychov, in *Advances in Photonic Materials and Devices* (Ed: S. Bhandarkar), John Wiley & Sons, New York **2012**.
- [30] M. L. Hair, W. Hertl, *J. Phys. Chem.* **1970**, 74, 91.
- [31] S. M. George, A. W. Ott, J. W. Klaus, *J. Phys. Chem.* **1996**, 100, 13121.
- [32] a) G. S. Higashi, C. G. Fleming, *Appl. Phys. Lett.* **1989**, 55, 1963; b) J. Lu, J. W. Elam, P. C. Stair, *Surf. Sci. Rep.* **2016**, 71, 410.
- [33] W.-T. Yao, S.-H. Yu, Q.-S. Wu, *Adv. Funct. Mater.* **2007**, 17, 623.
- [34] M. Dhanam, K. Balakrishnan, N. Jose, *Chalcogenide Lett.* **2009**, 6, 713.
- [35] a) F. Teng, Q. Liu, H. Zeng, *J. Colloid Interface Sci.* **2012**, 368, 512; b) A. Gaudin, D. Fuerstenau, M. Turkanis, *Trans. Am. Inst. Min. Metall. Eng.* **1957**, 208, 65.
- [36] a) J. T. Klopogge, L. V. Duong, B. J. Wood, R. L. Frost, *J. Colloid Interface Sci.* **2006**, 296, 572; b) J. Zähr, S. Oswald, M. Türpe, H. J. Ullrich, U. Füssel, *Vacuum* **2012**, 86, 1216.
- [37] M. R. Alexander, G. E. Thompson, G. Beamson, *Surf. Interface Anal.* **2000**, 29, 468.
- [38] a) W. M. Mullins, B. L. Averbach, *Surf. Sci.* **1988**, 206, 52; b) W. M. Mullins, B. L. Averbach, *Surf. Sci.* **1988**, 206, 41.
- [39] a) S. J. Kerber, J. J. Bruckner, K. Wozniak, S. Seal, S. Hardcastle, T. L. Barr, *J. Vac. Sci. Technol., A* **1996**, 14, 1314; b) N. D. Hoa, S. Y. An, N. Q. Dung, N. van Quy, D. Kim, *Sens. Actuators, B* **2010**, 146, 239.
- [40] D. Briggs, D. M. Brewis, M. B. Konieczko, *J. Mater. Sci.* **1979**, 14, 1344.
- [41] P. Persson, B. Malmensten, I. Persson, *J. Chem. Soc., Faraday Trans.* **1991**, 87, 2769.
- [42] a) V. Naumann, M. Otto, R. B. Wehrspohn, C. Hagendorf, *J. Vac. Sci. Technol., A* **2012**, 30, 04D106; b) L. G. Gosset, J.-F. Damlencourt, O. Renault, D. Rouchon, P. Holliger, A. Ermolieff, I. Trimaille, J.-J. Ganem, F. Martin, M.-N. Séméria, *J. Non-Cryst. Solids* **2002**, 303, 17.
- [43] S. Jakschik, U. Schroeder, T. Hecht, M. Gutsche, H. Seidl, J. W. Bartha, *Thin Solid Films* **2003**, 425, 216.
- [44] V. I. Mikhaylov, T. P. Maslennikova, P. V. Krivoschapkin, *Mater. Chem. Phys.* **2017**, 186, 612.
- [45] G. C. Correa, B. Bao, N. C. Strandwitz, *ACS Appl. Mater. Interfaces* **2015**, 7, 14816.
- [46] a) R. Goswami, C. S. Pande, N. Bernstein, M. D. Johannes, C. Baker, G. Villalobos, *Acta Mater.* **2015**, 95, 378; b) R.-S. Zhou, R. L. Snyder, *Acta Crystallogr., Sect. B Struct. Sci.* **1991**, 47, 617.
- [47] a) T. Koda, S. Shionoya, *Phys. Rev.* **1964**, 136, A541; b) S. Shigeo, E. Koh, K. Hirohiko, *Phys. Chem. Solids* **1965**, 26, 697; c) K. W. Böer, U. W. Pohl, *Semiconductor Physics*, Springer, Cham, Switzerland **2018**.

- [48] a) S. Shionoya, H. P. Kallmann, B. Kramer, *Phys. Rev.* **1961**, 121, 1607; b) R. H. Bube, *Phys. Rev.* **1950**, 80, 655.
- [49] a) K. Wenderich, G. Mul, *Chem. Rev.* **2016**, 116, 14587; b) O. Sacco, V. Vaiano, D. Sannino, R. A. Picca, N. Cioffi, *J. Colloid Interface Sci.* **2019**, 537, 671.
- [50] a) S. C. Chan, M. A. Barteau, *Langmuir* **2005**, 21, 5588; b) E. Pulido Melián, O. González Díaz, J. M. Doña Rodríguez, G. Colón, J. A. Navío, M. Macías, J. Pérez Peña, *Appl. Catal. B* **2012**, 127, 112.
- [51] a) S. K. Maji, A. K. Dutta, D. N. Srivastava, P. Paul, A. Mondal, B. Adhikary, *Polyhedron* **2011**, 30, 2493; b) J. Yu, J. Zhang, S. Liu, *J. Phys. Chem. C* **2010**, 114, 13642; c) X. Yu, J. Yu, B. Cheng, B. Huang, *Chem. - Eur. J.* **2009**, 15, 6731.
- [52] a) T. S. Natarajan, M. Thomas, K. Natarajan, H. C. Bajaj, R. J. Tayade, *Chem. Eng. J.* **2011**, 169, 126; b) E. T. Soares, M. A. Lansarin, C. C. Moro, *Braz. J. Chem. Eng.* **2007**, 24, 29; c) X. Qin, L. Jing, G. Tian, Y. Qu, Y. Feng, *J. Hazard. Mater.* **2009**, 172, 1168.